HHS Public Access

Author manuscript

Nat Cell Biol. Author manuscript; available in PMC 2019 October 15.

Published in final edited form as:

Nat Cell Biol. 2019 May ; 21(5): 603–613. doi:10.1038/s41556-019-0313-6.

Ultrastructure and dynamics of actin-myosin II cytoskeleton during mitochondrial fission

Changsong Yang and **Tatyana M. Svitkina***

Department of Biology, University of Pennsylvania, Philadelphia, PA 19104

Abstract

Mitochondrial fission involves preconstriction of the organelle followed by scission by dynamin-related protein Drp1. Preconstriction is facilitated by actin and nonmuscle myosin II through a mechanism that remains unclear, mostly, due to unknown cytoskeleton ultrastructure at mitochondrial constrictions. Here, using platinum replica electron microscopy, we show that mitochondria in cells are embedded into an interstitial cytoskeletal network containing abundant unbranched actin filaments. Both spontaneous and induced mitochondrial constrictions typically associate with a criss-cross array of long actin filaments that comprise a part of this interstitial network. Nonmuscle myosin II is found adjacent to mitochondria without specific enrichments at the constriction sites. During ionomycin-induced mitochondrial fission, F-actin clouds colocalize with mitochondrial constriction sites, whereas myosin II clouds mostly fluctuate nearby. We propose that myosin II promotes mitochondrial constriction by inducing stochastic deformations of the interstitial actin network, which applies pressure onto mitochondrial surface, thus initiating curvature-sensing mechanisms that complete mitochondrial constriction.

Keywords

Mitochondria; fission; endoplasmic reticulum; INF2; Drp1; ultrastructure; platinum replica electron microscopy; actin; nonmuscle myosin II

Introduction

Mitochondria in eukaryotic cells play key roles in energy production and cellular homeostasis. Proper regulation of mitochondrial fission and fusion is essential for mitochondrial health and, consequently, for cellular functions, whereas abnormal mitochondrial dynamics are linked to many human diseases including neurodegenerative, cardiac and metabolic disorders[1–3].

*Correspondence should be addressed to: Tatyana Svitkina, Department of Biology, University of Pennsylvania, 433 S. University Avenue, Philadelphia, PA 19104, USA, Tel.: (215) 898-5736, svitkina@sas.upenn.edu.

Author contributions

C.Y. performed all experimental work and data analyses; CY and TS made figures and wrote the manuscript.

Financial and non-financial competing interests

Authors have no financial and non-financial competing interests.

Mitochondrial fission is a multistep process[4]. A late step in this process is largely executed by the dynamin family GTPase, Drp1[5], although classical dynamin2 can also contribute[6]. The estimates of the intrinsic diameter of helical Drp1 oligomers that need to wrap around the mitochondrion to mediate fission vary significantly from only ~30 nm[7] to ~60 nm[8] to ~200 nm[9]. However, even with the upper estimate, the oligomer diameter seems insufficient to circumscribe typical mitochondria having diameters ≥200 nm. Therefore, Drp1 recruitment is thought to require preconstriction of the mitochondrion[10]. Prefission sites on mitochondria often associate with the endoplasmic reticulum (ER) prior to Drp1 recruitment[11]. Furthermore, mitochondrial preconstriction has been functionally linked to the actin cytoskeleton, specifically, to activities of two actin filament nucleators – formin INF2-CAAX[10] and Spire1C[12] – that reside on the ER and mitochondria, respectively. Association of INF2-CAAX with the ER can explain the ER contribution to mitochondrial constriction. Additional studies suggested that nonmuscle myosin II (NMII) also has fission-promoting roles[13,14].

A satisfactory mechanistic model that would explain the role of the actin cytoskeleton in mitochondrial constriction is still lacking. The actin cytoskeleton in cells can generate both pushing or pulling forces[15]. Therefore, one possibility is that polymerizing actin filaments push onto the mitochondrion to induce constriction. In cells, pushing force is usually generated by actin filaments nucleated by the Arp2/3 complex. However, no local enrichments of Arp2/3 complex was observed at mitochondrial constriction sites[16]. Alternatively, pushing force could be generated by actin filaments nucleated by INF2-CAAX off the ER surface[10] and/or by Spire1C off mitochondrial surface[12]. In both cases, however, actin filaments are predicted to abut the mitochondrion with their pointed ends, which is a rather unconventional mode of pushing force generation. Another possibility is that the actin cytoskeleton instead applies pulling force by employing NMII activity[17]. Along these lines, an apparently straightforward scenario is that NMII builds and constricts a circumferential actin ring around the mitochondrion, in analogy with cytokinesis[18]. A weakness of this model is that in order to generate contraction NMII assembles into ~300 nm long bipolar filaments[19,20]. This length is significantly larger than a typical mitochondrion diameter (~200 nm). Since NMII filaments do not exhibit any significant bending either in cells[20] or in vitro[19], the smallest “contractile ring” they can form would represent an equilateral triangle with the side length of 300 nm, which can constrict a mitochondrion down to a diameter of ~350 nm, but not smaller. These considerations make it geometrically challenging to employ an actin-NMII contractile ring to constrict mitochondria to a diameter suitable for Drp1 binding.

The mechanism of actin-dependent mitochondrial constriction might be understood if the actual structure of the actin cytoskeleton at mitochondrial constriction sites was known. For example, the presence of actin filaments abutting the mitochondrial constriction site with their ends at nearly right angles would favor the pushing model, whereas the presence of actin filaments circumscribing the constriction site would support the contractile ring model. The problem resides in availability of a technique capable of simultaneously revealing high resolution structure of the cytoskeleton and membrane organelles. Despite remarkable developments in superresolution fluorescence microscopy[21], single-filament resolution of the actin cytoskeleton so far is achievable only by electron microscopy (EM). Among

various EM approaches, only a few can properly preserve and resolve individual actin filaments. Platinum replica EM (PREM) has been particularly productive in this respect[22]. In PREM, a transmission electron microscope is used to visualize fine 3D topography of the sample, which is rotary-shadowed with a thin layer of platinum after detergent-mediated exposure of the cytoskeleton, fixation and critical point drying of the sample. Although critical point drying can lead to some shrinkage of the cell, the mutual arrangement of the intracellular structures remains largely preserved, as evidenced by correlative light microscopy and PREM[23–29]. However, detergent extraction would dissolve membrane organelles. Alternatively, the cell interior can be exposed by mechanical "unroofing" of cells[30,31]. Yet, most common unroofing protocols lead to a loss of most intracellular organelles including mitochondria.

Here, we have developed protocols to expose the cell interior while preserving both membrane organelles and the associated cytoskeleton and used PREM to reveal organization of the actin-NMII cytoskeleton at mitochondrial constriction sites. Our observations are not consistent with either the polymerization-mediated pushing or contractile ring models. Instead, they suggest that NMII-dependent stochastic contractions of the interstitial cytoskeletal network induce deformations of mitochondria, which eventually lead to mitochondrial constriction and fission.

Results

Visualization of Membrane Organelles and the Cytoskeleton by PREM

To reveal cytoskeletal organization at mitochondrial constriction sites by PREM, we tested various approaches to remove the apical plasma membrane, while preserving organelles and the associated cytoskeleton. Two most effective approaches in our hands were (1) extraction with a mild detergent saponin in cold (Fig. 1a–d and Supplementary Fig.1a–d) and (2) ripping off of the apical membrane by lightly attached nitrocellulose membrane (Fig. 1e, f and Supplementary Fig. 1e, f) (see Methods). Both methods produced openings in the apical surface, through which a nearly intact cell interior with membrane organelles could be visualized.

In successfully exposed interiors of glial cells in mixed cultures of dissociated rat hippocampal cells, mitochondria and the ER could be recognized by their distinctive morphology (Fig. 1 and Supplementary Fig. 1). Mitochondria often had an elongated tubular shape with smooth outlines and were characterized by relatively high electron density, probably, due to dense internal contents. Although PREM primarily reveals sample surface topography, the biological material retained underneath the metal layer creates additional contrast, especially after fixation with uranyl acetate. The ER, on the other hand, was more polymorphic and consisted of relatively translucent membrane structures, such as thin anastomosing tubules with irregular contours, as well as larger sacs and sheets. The shape and dimensions of ER components varied significantly, both within the cell and among different cells, so that sometimes the ER could be recognized only tentatively. The two complementary methods of opening up the cell – chemical extraction and mechanical rupture – produced similar results, suggesting that they faithfully report the overall organization of membrane organelles and the cytoskeleton in the cell interior. In subsequent

experiments, we mostly employed nitrocellulose-based unroofing, because it was faster and more efficient across different cell types.

To unambiguously identify mitochondria and the ER in unroofed PREM samples, we performed correlative light and electron microscopy (CLEM) of COS-7 cells transfected with the *mitochondrial marker* Mito-BFP, either alone (Fig. 2a–d) or in combination with the ER marker mCherry-Sec61β (Figure 2e–h). In our culture conditions, most mitochondria in COS-7 cells, either unroofed (Fig. 2) or living (Fig. 3a), were short, and only few of them had a typical elongated shape. CLEM showed that morphologically identifiable mitochondria colocalized with the Mito-BFP-labeled structures visualized by confocal microscopy. Similarly, a network of thin electron-translucent tubules visible in the PREM images closely matched the fluorescently labeled ER network in confocal images of the same cells (Fig. 2). These results validate our morphology-based identification of mitochondria and the ER in PREM samples.

Structural Organization of the Cytoskeleton and ER around Mitochondria

We observed different modes of ER-mitochondria interaction in glial cells (Fig. 1), which could be better appreciated in 3D views of PREM stereo pairs (Supplementary Fig. 1b–d,f). ER tubules could cross a mitochondrion at different angles forming underpass or overpass intersections. ER tubules could end at the mitochondrion or wrap around it. We defined constrictions as sites, at which the width of a mitochondrion decreased by ≥20%. Most of the ER-mitochondrion interactions (95%, 355 sites in 92 cells from 6 independent experiments) occurred at unconstricted mitochondrial sites, while some ER tubules could contact a mitochondrion close to a constriction site (Fig. 1b, c, white arrows). On the other hand, a fraction of mitochondrial constrictions intersected by ER tubules was ~75% (N=111), consistent with the reported light microscopy data[11]. An average length of mitochondrial constrictions measured between half-maximal widths on each side of the constriction was 701±21 nm (mean±SEM; N=113 constrictions from 10 cells), when estimated from fluorescence images, and 763±24 (N=132 constrictions from 37 cells) when measured using PREM images. Similarity of these values (p=0.11, two-tailed nonparametric Mann-Whitney test) further argues for proper preservation of the mitochondrial shape in the course of PREM preparation.

Both mitochondria and the ER were entangled with the cytoskeleton, which formed a loose 3D network in the cell interior. This network predominantly consisted of actin filaments, but also included microtubules and intermediate filaments that could be recognized by their distinct thicknesses. Some actin filaments comprising this interstitial network appeared to emanate from the ER and could extend to mitochondria or another ER structure (Fig. 1d, f, green). Less frequently, actin filaments appeared to originate at the mitochondrial surface (Fig. 1f, red). Most actin filaments in the interstitial network appeared unbranched (no detectable branches over visible length), although occasional branched actin filaments could be detected (Fig. 1f, blue). Importantly, we did not encounter at the mitochondrial surface the stereotypical bush-like networks of short branched filaments, which are characteristic for sites of intense Arp2/3 complex-dependent nucleation[23,32]. The lengths of actin filaments in the interstitial network measured over distances, which allowed us to clearly visualize

individual filaments between their overlaps with other structures, was 203±91 nm (mean ±SD; n=535 filaments in 12 cells from 2 independent experiments). This result is close to the observed ~270 nm length of actin filaments assembled in vitro in the presence of constitutively active INF2 and profilin[33]. We cannot exclude a possibility that very short filaments not incorporated into larger cytoskeleton systems could be lost as a result of opening up the cell interior. However, such filaments, if they exist, are poorly suited for force generation because they would be unable to gain traction without associating with more stable structures.

The mitochondrial constriction sites were not frequent in these cells, consistent with relatively infrequent fission events at steady state[10]. However, the actin filament density appeared to be greater at mitochondrial constrictions defined as described above (20.8±1.8 μm/μm^2; mean±SEM; n = 12 constrictions with total area of 0.88 μm^2 in 6 cells from 3 independent experiments) than at adjacent regions on both sides of the constriction (5.2±0.9 μm/μm^2; n = 24 regions with total area of 1.8 μm^2; $p<0.0001$; paired t-test) (Fig. 1b, c, f). Notably, these actin filaments exhibited neither end-on abutting nor circumferential orientation, which could be predicted by the pushing-based and contractile ring-based models, respectively. Instead, the actin filaments from the interstitial network intersected the mitochondrial constriction sites at a variety of angles, but mostly diagonally (Fig. 1b,c,f). Another conspicuous feature of mitochondria-cytoskeleton interactions was that a fraction of mitochondrial ends (9%, n=355 ends) was tightly associated with an array of actin filaments, which was denser than at the adjacent mitochondrial regions (Fig. 1b, white arrowhead).

Together, these results do not support an existence of mitochondrion-associated actin arrays that would be specifically dedicated to generating mitochondrial constriction. Instead, our observations raise a possibility that actin-dependent promotion of mitochondrial constriction could be mediated by actin filaments from the interstitial cytoskeletal network.

Organization of the Cytoskeleton at Mitochondrial Constriction Sites after Inhibition of the Drp1-Mediated Scission

The low intrinsic frequency of mitochondrial fission is a challenge for our PREM analysis, because of a low probability that two rare events – mitochondrion fission and proper unroofing – would occur at the same location. This problem also raises a concern that we might miss the constriction-specific actin arrays. Therefore, we used expression of a dominant negative Drp1 mutant, Drp1-K38A[34], which blocks mitochondrial fission[8,35,36], but is not expected to affect the cytoskeleton-dependent preconstriction mechanisms. Therefore, frequency of mitochondrial constrictions should be increased in such cells.

We used a construct that simultaneously expresses shRNA against endogenous Drp1 and shRNA-insensitive GFP-Drp1-K38A. Expression of GFP-Drp1-K38A in COS-7 cells, which normally have short mitochondria, resulted in the formation of many elongated mitochondria (Fig. 3a,b), likely due to stalled fission. PREM analysis of these cells revealed multiple constrictions along the length of elongated mitochondria (Fig. 3c–h). Actin filaments at the mitochondrial constriction sites again formed denser arrays (18.3±2.1 μm/μm^2; mean±SEM; n = 49 constrictions with total area of 4.2 μm^2 in 21 cells from 3 independent experiments) than at the neighboring mitochondrial regions (4.1±0.4 μm/μm^2; n = 98 constrictions with

total area of 7.7 μm^2; $p<0.0001$; Wilcoxon two-tailed paired test). Most actin filaments were unbranched, but some branched filaments were also present (Fig. 3e). Actin filaments could be oriented along, across or diagonally relative to the mitochondrion axis (Fig. 3f–h). Highly constricted sites tended to be associated with diagonal actin filaments, which criss-crossed the constriction site above and below the mitochondrion (Fig. 3g,h and Supplementary Fig. 4; Supplementary Video 1). We sometimes observed that a mitochondrion formed a prominent bulge near the constriction site (Fig. 3c and Supplementary Fig. 4), as if experiencing longitudinal pressure from the constriction area. More shallow mitochondrial constrictions had less distinct criss-cross orientation of actin filaments at the constriction site (Fig. 3e,f). We again observed a fraction of mitochondrial ends associating with relatively dense actin filaments, which contain both unbranched and branched actin filaments (Fig. 3e). The ER could closely interact with the mitochondrion or be located at a distance from it, both at the constriction sites and at actin-enriched mitochondrial ends. Some actin filaments that associate with the mitochondrion in these cases appeared to extend from the nearby ER, whereas filaments that apparently originated at the mitochondrial surface were also present (Fig. 3c,f, red).

Thus, despite significantly increased constriction frequency after expression of the dominant negative Drp1, the actin cytoskeleton at mitochondrial constriction sites still appeared to be a part of the interstitial cytoskeletal network, rather than a specialized actin array.

Constitutively Active INF2-CAAX Induces Abundant Actin Filaments at the ER Surface

Frequent instances of actin filaments emanating from the ER, including those extending toward mitochondria, support the idea that actin filaments involved in mitochondrial constriction are nucleated, at least in part, by the ER-associated INF2-CAAX[10]. A constitutively active form of INF2-CAAX, INF2-A149D-CAAX, induces actin assembly at the ER in U2OS cells[37] and stimulates mitochondrial fission[10]. To determine the precise localization and ultrastructural organization of actin filaments induced by INF2-A149D-CAAX, we used COS-7 cells transfected with INF2-A149D-CAAX for confocal and PREM analyses (Supplementary Fig. 3).

In COS-7 cells coexpressing GFP-INF2-A149D-CAAX, mCherry-Sec61β, and BFP-Mito and stained with Alexa 680-phalloidin to detect F-actin, GFP-INF2-A149D-CAAX colocalized with a subset of ER structures, usually, with abnormally thick ER tubules. F-actin in these cells was enriched specifically at the GFP-INF2-A149D-CAAX-positive ER components, but also extended from these regions into interstitial space and could reach mitochondria (Supplementary Fig. 3a–c).

Using CLEM of COS-7 cells transfected with mCherry-INF2-A149D-CAAX we found that the mCherry-INF2-A149D-CAAX-positive ER-like structures were densely covered with actin filaments (Supplementary Fig. 3d–h). As expected for formin-mediated nucleation, most of these filaments were long and unbranched. They typically ran along the ER tubule as a loose bundle (Supplementary Fig. 3h), although randomly oriented actin filaments extending from the ER into adjacent areas and toward mitochondria were also observed (Supplementary Figs. 3h, 4).

Expression of INF2-A149D-CAAX stimulates mitochondrial fission in U2OS cells[14]. Considering that mitochondria in COS-7 cells are already short, the mitochondrial constriction sites in mCherry-INF2-A149D-CAAX-expressing cells were undetectable by PREM. Therefore, we expressed mCherry-INF2-A149D-CAAX in COS-7 cells that three days earlier were transfected with GFP-K38A-Drp1 to inhibit mitochondrial fission (Fig. 4). Confocal microscopy of double-expressing cells (Fig. 4a) showed an ER-like distribution of mCherry-INF2-A149D-CAAX, as well as GFP-K38A-Drp1 aggregates[34] and faint puncta.

As in cells with single INF2-A149D-CAAX transfection (Supplementary Fig. 4), CLEM of double transfected cells showed numerous long actin filaments associated with the mCherry-INF2-A149D-CAAX-positive ER structures. At low magnification, mitochondria in these cells appeared short and round (Fig. 4c). However, high magnification views showed that they were connected by thin bridges, some of which were marked by faint GFP-K38A-Drp1 puncta (Fig. 4d,e). The presence of long mitochondria with “bead-on-a-string” morphology due to multiple constrictions allowed us to identify double-transfected cells even by non-correlative PREM (Fig.4f,g). The mitochondrial constrictions in double transfected cells were significantly deeper (Fig. 4), as compared with the cells expressing K38A-Drp1 alone (Fig. 3), suggesting that extensive actin polymerization induced by constitutively active INF2-CAAX enhances mitochondrial constriction. These narrow mitochondrial constrictions were crossed by unbranched actin filaments, some of which could be traced back to ER structures, whereas other filaments had no obvious connection with the ER. The population of actin filaments extending from the ER toward a mitochondrial constriction represented only a small fraction of the ER-associated filaments (Figure 4d–f). The mixed origin of constriction-associated actin filaments suggests that INF2-A149D-CAAX can enhance mitochondrial constriction by producing more interstitial actin filaments, which then can be stochastically used for mitochondrial constriction.

Organization of the Cytoskeleton at Mitochondrial Constriction Sites after Drug-Induced Mitochondrial Fission

Several drugs have been used previously to stimulate mitochondrial fission, including the electron transport chain complex I inhibitor rotenone[38,39] and the calcium ionophore ionomycin[36,40]. We analyzed rotenone-treated glial cells by confocal microscopy and PREM.

As revealed by fluorescence microscopy of a mitochondrial marker Tom20-mCherry, mitochondrial constriction and fission were efficiently induced by rotenone treatment (Fig. 5a). PREM showed that mitochondria in cells unroofed 8–20 min after rotenone application contained many constriction sites, which were often associated with a criss-cross array of actin filaments extending from the surrounding interstitial network and sometimes attached to putative ER components located nearby (Fig. 5b–e). Actin filaments could also intersect a mitochondrion at other places, whereas mitochondrial ends were often associated with relatively dense actin filaments, some of which extended from adjacent ER segments (Fig. 5b,d). Overall, the cytoskeleton organization at the rotenone-induced mitochondrial constrictions was similar to that observed at less frequent constrictions in untreated cells,

although mitochondria in rotenone-treated cells appeared to be more extensively intertwined with the cytoskeleton.

Since PREM images gave an impression of a higher density of the interstitial actin network after rotenone treatment relative to basal conditions (see Fig. 1), we monitored rotenone-induced changes in F-actin density in live HeLa cells expressing an F-actin reporter GFP-Ftractin and Mito-BFP. Imaging was performed at the cell midplane along the Z-axis to specifically observe F-actin in the cytoplasm away from abundant cortical F-actin. Rotenone treatment induced F-actin assembly in the cytoplasm and progressive mitochondrial fission (Fig. 5f–h, Supplementary Video 2). Moreover, the newly formed F-actin structures exhibited substantial overlap with mitochondria (Fig. 5g), raising an intriguing possibility that rotenone induces actin polymerization off mitochondria. The rotenone-induced F-actin signal most likely corresponded to the interstitial actin network observed by PREM in the cell interior, suggesting a role of drug-induced actin accumulation in the enhanced mitochondrial fission.

Dynamics of Cytoplasmic F-actin and NMIIA at Mitochondrial Fission Sites

The diagonal criss-cross pattern of unbranched actin filaments that was often observed at mitochondrial constriction sites could form effective tracks for myosin motors. Considering that NMII stimulates mitochondrial fission[14,36], we examined localization and dynamics of NMII during ionomycin-induced mitochondrial fission.

For live cell imaging, HeLa cells were triple-transfected with Mito-BFP, mCherry-NMIIA and GFP-Ftractin (Fig. 6). Ionomycin treatment has been shown to stimulate F-actin assembly in the cytosol[36] due to INF2-CAAX activation at the ER[41]. Accordingly, we observed significant accumulation of F-actin in the cytoplasm after ionomycin application (Fig. 6a,b) and partial colocalization of this cytoplasmic F-actin with the ER (Supplementary Figure 5a, Supplementary Video 3). Additionally, ionomycin treatment induced a significant increase in the fluorescence intensity of NMIIA in the cytoplasm, which slightly lagged behind the increase of F-actin (Fig. 6a,b). The mitochondrial lengths decreased in parallel with accumulation of F-actin and NMIIA in the same cells (Fig. 6b), supporting the idea that increased density of the interstitial actin-NMII network correlated with mitochondrial fission.

Detailed analysis of time-lapse sequences showed that initial mitochondrial constrictions were usually accompanied by arrival of an F-actin cloud that traversed the mitochondrion at the constriction site. Although these clouds exhibited dynamic behavior, they usually remained at the constriction site until the fission occurred (Fig. 6c and Supplementary Fig. 5b; Supplementary Videos 4, 5). These F-actin clouds likely corresponded to the criss-cross arrays of actin filaments at mitochondrial constriction sites revealed by PREM. Clouds of NMIIA also fluctuated around mitochondria during their constriction and fission and could occasionally overlap with the constriction site. However, most of the time, the NMII clouds flanked the mitochondrion rather than overlapped with it (Fig. 6c, Supplementary Fig.5b, Supplementary Videos 4, 5).

We also analyzed the dynamics of another NMII isoform, NMIIB, during mitochondrial fission in COS-7 cells, which have NMIIB as their major NMII isoform[42]. In COS-7 cells expressing GFP-NMIIB, mCherry-Ftractin and Mito-BFP, ionomycin treatment induced F-actin assembly and mitochondrial fission (Supplementary Fig. 6, Supplementary Video 6). The observed behavior of NMIIB and F-actin clouds at mitochondrial fission sites in these cells was similar to those described for HeLa cells and NMIIA (Fig. 6 and Supplementary Fig. 5).

These data show that during ionomycin-induced mitochondrial fission, NMII does not exhibit specific enrichments at mitochondrial constrictions, as would be expected for contractile ring-mediated force generation. Instead, the NMII signals fluctuate in the vicinity of the mitochondrion suggesting that NMII exerts force from the mitochondrial neighborhood to stimulate constriction, but does not specifically accumulate at the constriction sites.

Functions and Ultrastructural Organization of NMII at Mitochondrial Constriction Sites

Inhibition of NMII activity in U2OS cells has been previously shown to result in elongation of mitochondria, suggesting impaired fission[14]. We evaluated roles of NMII in mitochondrial constriction using NMII inhibitors (Fig.7a–c). Untreated or DMSO-treated COS-7 cells expressing GFP-K38A-Drp1 exhibited long mitochondria with multiple constrictions (Fig. 7a, left). Treatment with an inhibitor of NMII ATPase blebbistatin (Fig. 7a, middle) or an inhibitor of myosin light chain kinase ML-7 (Fig. 7a, right) resulted in dramatic relaxation of constrictions, as validated by quantification of constriction depths (Fig.7b). Live cells imaging of COS-7 cells expressing GFP-K38A-Drp1 also demonstrated rapid relaxation of pre-existing constrictions after ML-7 treatment (Fig.7c).

To determine NMII localization at mitochondrial constriction sites at high resolution, we performed immunogold PREM with an NMIIA antibody of unroofed ionomycin-treated HeLa cells (Figure 7d–f and Supplementary Video 7). The NMIIA immunogold particles, as expected, were associated with actin filaments throughout the cell. Although some gold particles could be present exactly at the mitochondrial constriction site, we did not detect an enrichment of NMIIA at mitochondrial constrictions. In fact, the average density of gold particles at mitochondrial constrictions (103±40 per μm^2; mean±SD; n=20 regions with total area of 1.2 μm^2 in 7 cells from 2 independent experiments) was slightly lower than the average density of gold particles associated with actin networks surrounding mitochondria (116±42 per μm^2; N=20 regions with total area of 3.9 μm^2 from 7 cells; p=0.0083, Wilcoxon paired two-tailed test). In cases when a constriction site was crossed by actin filaments, NMIIA immunogold tended to concentrate on these intersecting actin filaments, usually on one or both sides from the mitochondrial constriction and only occasionally overlapping with the constriction (Fig. 7e). Similarly, immunogold staining of COS-7 cells with NMIIB antibody did not show an enrichment of NMIIB at mitochondrial constriction sites (Supplementary Fig.6c), although the overall density of NMIIB staining was significantly lower. The specificity of NMII immunogold staining was validated previously[43]. As additional controls, we stained COS-7 cells with the secondary antibody only, or with NMIIA antibody, which should not recognize any endogenous proteins in this cell type.

These control samples contained 1.4±0.2 (mean±SEM; N=25 cells) and 1.7±0.2 (N=11 cells) particles per μm^2, respectively, which were not significantly different from each other ($p=0.73$, Games-Howell's posthoc multiple comparisons test), but dramatically lower than in HeLa cells stained with NMIIA antibody (100±8 particles per μm^2; N=44 cells; $p<0.0001$; Welch's Anova test), demonstrating high specificity of staining. These data suggest that in both HeLa and COS7 cells NMII contributes to mitochondrial constriction without formation of a contractile ring, but by acting as a part of the surrounding interstitial network. Most likely, NMII applies tension to interstitial actin filaments that cross the mitochondrion.

Discussion

Insufficient structural information about actin organization at mitochondrial constriction sites precluded formulation of an explicit model for actin-stimulated mitochondrial constriction. To overcome this bottleneck, we have developed an optimized PREM protocol to visualize both membrane organelles and the cytoskeleton in an apparently intact state. Although we cannot exclude occasional ruptures, the similarity of the intracellular organization after chemical (saponin extraction) and mechanical (nitrocellulose sheets) exposure suggests that the extent of potential damage is relatively minor.

The two major models of actin-dependent mitochondrial constriction predict specific organization of actin filaments at mitochondrial constrictions (see Introduction). However, our PREM data are not consistent with these predictions. We mostly observe diagonally oriented unbranched actin filaments that intersect the mitochondrion near constriction sites. At relatively deep mitochondrial constrictions, the diagonal actin filaments appeared rather straight and taut, as if they were under tension, and are often associated with NMII. Branched actin filaments, although present, were not abundant at the mitochondrial surface, consistent with the reported lack of effects of Arp2/3 inhibition on mitochondrial lengths[14]. The reported positive roles of the Arp2/3 complex in mitochondrial fission[16] can be potentially explained by contribution of Arp2/3-dependent nucleation to the formation of the interstitial actin network.

Our data suggest the following mechanistic model for actin-mediated mitochondrial constriction (Fig. 7d). In the cytoplasm, mitochondria are suspended in the interstitial cytoskeletal network, which is formed primarily by unbranched actin filaments, but also contains NMII filaments, microtubules and intermediate filaments. We suggest that contractile activity of NMII causes stochastic inhomogeneous deformations of this interstitial network, such as stretching, bundling and twisting. A mitochondrion trapped in this mechanically active network can be locally squeezed between taut actin filaments, which would cause local invaginations in the mitochondrial surface, which is likely a pivotal point for initiating mitochondrial constriction. This idea is supported by recent findings that mitochondrial fission can be induced by force application in the absence of the ER or functional actin network[44]. The underlying mechanism was proposed to include accumulation of the curvature-sensing mitochondrial fission factor (Mff) at the initial invagination and subsequent propagation of the invagination into a constriction via curvature-inducing Mff properties[44]. Since Mff is a mitochondrial receptor for Drp1, the constriction-enriched Mff then recruits Drp1 to execute scission.

In the context of our model, NMII can pull on actin filaments intersecting the mitochondrion from a distance. This process can be distantly compared to how pulling on the corset strings can cause constriction of a waistline. NMII filaments are likely more efficient if they localize in the mitochondrial neighborhood. Otherwise, force would be absorbed by network deformations in the intervening space. Accordingly, we often see fluctuating NMII clouds in the vicinity of constricting mitochondria. A positive correlation between accumulation of the cytoplasmic F-actin induced by ionomycin[36,41] or rotenone (this study) and the drug-induced frequency of mitochondrial fission[36,38,39] can be explained by a greater probability for a mitochondrion to be deformed by a denser interstitial actin-NMII network. The origin of interstitial actin filaments may not be critically important. For example, ionomycin induces actin polymerization through ER-associated INF2-CAAX[41], whereas rotenone-induced F-actin assembly might potentially involve regulation of the mitochondrion-anchored Spire1C[12].

The stochastic nature of our model does not exclude some degree of specificity for the location of constriction sites. For example, a cross-talk between INF2-CAAX and Spire1C at ER-mitochondria juxtapositions[10–12] can induce local network densities and increase the chance of constriction. The internal organization of the mitochondrion can also be a contributing factor. Thus, mitochondrial fission often occurs near a nucleoid[45], probably, because nucleoid-containing segments of mitochondria are denser, as can be inferred from nucleoid recovery from bottom fractions of density gradients[46,47], and therefore likely stiffer. If so, then tense actin filaments could “slip” to the adjacent softer regions, where they could induce deformation. Similarly, in cases when the inner mitochondrial membrane is constricted before the outer membrane[48,49] the separation of two mitochondrial membranes may locally soften the mitochondrion and make this site more susceptible to deformation.

In conclusion, using newly developed PREM protocol, we have revealed structure of the cell interior containing both membrane organelles and the cytoskeleton. Our data suggest a mechanism of actin-dependent mitochondrial constriction, in which stochastic deformations of the mechanically active interstitial actin network generates force required for this process.

Materials and methods

Cell culture

Primary dissociated cell cultures from embryonic rat hippocampi isolated as described previously[50] were obtained from the MINS Neuron Culture Service Center (University of Pennsylvania, Philadelphia, PA) and cultured as described previously[51]. In brief, hippocampi were dissected from brains of Sprague-Dawley rat embryos at embryonic day 18–20 and dissociated into individual cells by incubating in a trypsin-containing solution. The cell suspensions containing both glial cells and neurons were plated on poly-L-lysine-coated (1 mg/ml, #P6282, Sigma) glass coverslips at a concentration of 150,000 cells per 35-mm dish in 1.5 ml neurobasal medium (Gibco) with 2% B27 supplement and cultured for 7–14 days. Only glial cells were used for experiments.

COS-7 and HeLa cells were cultured in Dulbecco’s modified Eagle’s medium (DMEM) supplemented with GlutaMAX (#10–569-010, Gibco), 10% fetal bovine serum (FBS) and

1% penicillin/streptomycin at 37 °C and 5% CO2. For drug treatment, rotenone (#R8875, Sigma) was used at 250 ng/ml for glial cells and at 750 ng/ml for HeLa cells. Ionomycin (#I0634, Sigma) was used at 4 μM.

Exposure of the cell interior for PREM

For saponin-mediated extraction, cells on glass coverslips were transferred into a pre-chilled to 4°C solution of 0.01% saponin [#47036, Sigma] in PEM buffer (100 mM PIPES-KOH, pH 6.9, 1 mM $MgCl_2$, and 1 mM EGTA) containing 2 μM unlabeled phalloidin [#P2141, Sigma], protease inhibitor cocktail (#I37786, Sigma) and 300 mM sucrose. After incubation on ice for 7 min, the cells were fixed with 2% glutaraldehyde [#01909, Polysciences] in 0.1 M Na-cacodylate buffer (pH 7.3) at room temperature for 20 min.

For mechanical unroofing, COS-7 and HeLa cells were seeded on coverslips coated with poly-D-lysine (0.2 mg/ml) or HistoGrip (Thermo Fisher Scientific, #008050) and cultured for 1–3 days. Neuronal cells were cultured as described above. A piece of nitrocellulose filter membrane (0.8 μm pore size; #AABPC5000, EMD Millipore) was soaked in PEM buffer containing 2 μM phalloidin and 10 μM taxol (#T7402, Sigma) and placed onto a wet 3MM filter paper to remove extra buffer and prevent from fast drying. A coverslip with cells was briefly dipped into PEM buffer with phalloidin and taxol. The excess buffer was removed by touching a piece of filter paper with the coverslip edge, and the coverslip was placed cell side down onto the nitrocellulose membrane for about 10 sec. Then, gentle pressure was applied to one corner of the coverslip to generate a gradient of nitrocellulose-cell adhesion, and thus produce properly unroofed cells somewhere along this gradient. The coverslip was then lifted from the nitrocellulose membrane and immediately placed into 0.2% glutaraldehyde solution in 0.1 M Na-cacodylate buffer for fixation. After evaluation of the unroofing quality by phase contrast microscopy, the samples were post-fixed with 2% glutaraldehyde.

As a control for potential damages caused by our unroofing procedure, we confirmed that incubation of living cells in the cytoskeletal buffer for over 5 min, much longer than a time period of ~30 sec required for nitrocellulose application and detachment, does not cause any apparent aberrations in the organization and dynamics of mitochondria and the actin cytoskeleton (Supplementary Fig. 2a). We also found that the morphology of the fluorescently labeled ER and mitochondria was similar in unroofed and not unroofed cells from the same CLEM preparations and also was comparable to control cells not subjected to the unroofing procedure (Supplementary Fig. 2b).

PREM and CLEM

Sample processing for regular and immunogold PREM and for CLEM was performed as described previously[52,53]. In brief, glutaraldehyde-fixed cells were post-fixed by sequential treatment with 0.1% tannic acid and 0.2% uranyl acetate in water, critical-point dried, coated with platinum and carbon, and transferred onto EM grids for observation.

For immunogold staining, unroofed unfixed cells were incubated for 30 min with NMIIA (#BT-567, BTI) or NMIIB (#3404, Cell Signaling) antibody diluted 1:20 in PEM buffer with phalloidin and taxol, washed with PEM buffer, and fixed with 0.2% glutaraldehyde. After

quenching with 2 mg/ml $NaBH_4$ in PBS for 10 min, cells were blocked with 1% BSA in buffer A (20 mM Tris-HCl, pH 8.0, 0.5 M NaCl, and 0.05% Tween-20), incubated with secondary antibodies conjugated with 12 nm or 18 nm colloidal gold (#711-205-152 and #711-215-152, respectively; Jackson ImmunoResearch) and, after washing, fixed with 2% glutaraldehyde and processed for PREM. The specificity of NMII antibodies has been previously validated using knockdown of either NMIIA or NMIIB in both immunofluorescence and Western blotting assays[54].

For CLEM, COS-7 cells expressing fluorescent protein(s) were grown on home-made coverslips with fiducial marks that were coated with poly-D-lysine or Histogrip. After nitrocellulose-mediated unroofing, cells were fixed with 0.2% glutaraldehyde, quenched with 2 mg/ml $NaBH_4$ in PBS and washed with PBS. For fluorescence microscopy, coverslips were placed with cell side down into glass-bottomed dishes and imaged by epifluorescence or spinning disk confocal microscopy with 100x objective. Then, the samples were post-fixed with 2% glutaraldehyde and processed for PREM.

PREM samples were examined using JEM 1011 transmission EM (JEOL USA, Peabody, MA) operated at 100 kV. Images were acquired by an ORIUS 832.10W CCD camera (Gatan, Warrendale, PA) and presented in inverted contrast. Stereo pairs were acquired at ±11° tilt angles and combined into a red-cyan anaglyph image using Adobe Photoshop software. Use red-cyan anaglyph glasses with red eye at left to visualize a stereo image. Correlative light microscopy and PREM images were aligned using Adobe Photoshop by rotating and proportionally enlarging fluorescence images until best match of individual cell regions is achieved. Because of sample shrinkage after critical point drying, perfect alignment of whole cells could not be achieved, but images of smaller cell regions could be reliably matched.

Plasmids and transfection

Mito-BFP (Addgene plasmid # 49151) and mCherry-Sec61β (Addgene plasmid #49155) were gifts from Dr. Gia Voeltz. Tom20-mCherry[55] was a gift from Dr. Andrew G. York (NIH, Bethesda, MD). The GFP-Drp1-K38A construct expressing the H1 promoter-driven shRNA for endogenous Drp1, as well as GFP(A206K)-tagged, RNAi-resistant rat Drp1(K38A)[56], was a gift from Dr. Henry Higgs (Dartmouth Medical School, Hanover, NH). GFP-Ftractin plasmid[57] was a gift from Dr. Michael Schell (Uniformed Services University, Bethesda, MD). mCherry-NMIIA encoding heavy chain of human NMIIA[58] was a gift from Dr. Venkaiah Betapudi (Addgene plasmid #35687). GFP-NMIIB encoding heavy chain of human nonmuscle myosin IIA[59] was a gift from Dr. Robert Adelstein (Addgene plasmid #11348). The mCherry-INF2-A149D-CAAX construct was prepared by recloning of INF2-A149D-CAAX from the GFP-INF2-A149D-CAAX construct (a gift from Dr. Henry Higgs)[60] into mCherry-C1 vector (Clontech).

Transient cell transfection was performed using Lipofectamine® LTX with Plus™ Reagent (Invitrogen). For transfection, cells were cultured for 6–16 h after plating and used at ~80% confluency. Transfected cells were used between 36 h and 60 h after transfection, except for cells transfected with mCherry-INF2-A149D-CAAX or GFP-INF2-A149D-CAAX, which were used within 24 hr after transfection. For double transfection with GFP-K38A-Drp1 and

mCherry-INF2-A149D-CAAX, cells were first transfected with GFP-K38A-Drp1. After 3 days, cells were replated onto coverslips and 6 h after plating transfected with mCherry-INF2-A149D-CAAX for 16 h before unroofing.

Fluorescence microscopy

For staining of F-actin with Alexa Fluor 680 phalloidin (#A22286, Thermo Fisher Scientific; 1:150 in PBS) cells were fixed with 0.2% glutaraldehyde, quenched with NaBH4 in PBS for 3 times, and permeabilized with 0.1% saponin in PBS for 5 min. Stained samples were mounted with ProLong Diamond Antifade Mountant (#P36961, Thermo Fisher Scientific).

For live-cell imaging, cells were cultured in the glass-bottomed MatTek dishes in phenol red-free Leibovitz's L-15 medium (#21083027, Gibco) supplemented with 1% FBS and maintained during observation at 37°C in humidified atmosphere using an UNO stage-top incubator (Okolab). For treatment with ionomycin or rotenone during live cell imaging, the drugs were first diluted in 200 μl of pre-warmed medium to 10-fold of the final concentration and added to the dish with cells containing 1.8 ml medium.

Epifluorescence microscopy was performed using Eclipse TE2000-U inverted microscope (Nikon) equipped with Planapo 100×1.3 NA objective and Cascade 512B CCD camera (Photometrics) driven by Metamorph imaging software (Molecular Devices). Spinning disk confocal microscopy was performed using Eclipse TiE inverted microscope (Nikon) equipped with a CSUX1 spinning disk (Yokogawa Electric Corporation), CFI60 Apochromat TIRF 100 × 1.49 NA oil objective, QuantEM 512SC digital camera (Photometrics), and perfect focus system driven by Nikon (NIS)-Elements Advanced Research software (Version 4.50). The 405-nm laser and ET455/50M filter were used for BFP; the 488 nm laser and 525/36 filter for GFP; the 561 nm laser and 605/70 filter for RFP; and 640 nm laser and 700/75 filter for Alexa Fluor 680. Time lapse sequences were acquired at rates ranging from 10 sec to 2 min per frame. To minimize photobleaching, low laser power and exposure times and a digital gain were used. 3D reconstructions of confocal stacks were generated from 3–5 consecutive Z-slices with a thickness of 0.2–0.3 μm using the alpha blending option in NIS-Elements software.

To determine effects of inhibition of NMII activity on mitochondrial constriction, COS-7 cells expressing GFP-K38A-Drp1 and Mito-BFP were treated with DMSO (D2650, Sigma) as control, or 50 μM blebbistatin (B592500, Toronto Research Chemicals) or 50 μM ML-7 (I715000, Toronto Research Chemicals) for 1 hour, fixed with 4% formaldehyde in PBS and imaged with spinning disk confocal microscopy. An extent of mitochondrial constriction was determined using Mito-BFP fluorescence intensity profiles generated using Plot Profile tool of ImageJ software after subtracting background. Profiles of average fluorescence intensity were generated using lines drawn along the mitochondrial long axis and spanning the mitochondrial width. The mitochondrial constriction index (MCI) was calculated using the following equation:

$$MCI = \left[1 - \frac{Imin}{1/2(Imax1 + Imax2)}\right] x100\%$$

Where *Imin* is the local minimum of fluorescence intensity and *Imax*1 *and Imax*2 are local fluorescence intensity maxima within 0.4 – 2 μm on each side from the local minimum. MCI is close to 100% for minimally constricted regions and decreases progressively with the extent of constriction.

Data analyses

For quantification of localization of mitochondria-ER overlaps relative to mitochondrial constrictions in PREM images, a distance of ≤100 nm between the narrowest part of the mitochondrion and the closest edge of the ER was considered to represent colocalization of the ER with the mitochondrial constriction. To measure actin filament lengths within interstitial cytoskeletal network, individual filaments having ~10 nm diameter (including platinum coating), which corresponds to actin filaments, were traced with a line tool in ImageJ for as long as they could be distinguished from the neighboring or overlapping filaments. Very short filaments (<50 nm) were ignored for this quantification. For evaluation of actin filament densities at mitochondrial constriction sites, an area of mitochondrial constriction was defined as extending from the narrowest region of the mitochondrion to half-maximal width of the adjacent unconstricted regions on both sides of the constriction, whereas mitochondrial regions beyond this boundary were selected for determination of actin filament densities at adjacent unconstructed mitochondrial regions. The total length of all actin filaments within selected regions was measured using the ImageJ line tool and normalized to the area of the region of interest. For quantification of NMII immunogold densities at mitochondrial constriction sites, an area of mitochondrial constriction was defined the same way. The regions of the surrounding interstitial network were selected near the constricted mitochondrion, but not overlapping with it and excluding other membrane structures in the region. The number of immunogold particles was counted and normalized to the area of the region of interest.

The time course of F-actin or NMIIA accumulation following drug treatments was assessed based on cumulative fluorescence intensities of respective markers (Ftractin or NMIIA) in confocal slices with a total width of 0.9–1 μm taken from the midplane of the cells. Average fluorescence intensities after background subtraction were determined for three regions of interest located away from the nucleus and the cortical region for each cell and time point and normalized against an average fluorescence intensity before drug treatment for each individual cell. The changes in the mitochondrial lengths after ionomycin treatment were monitored for individual mitochondria over time. Only easily distinguishable mitochondria longer than 0.5 μm were measured.

Statistics and reproducibility

Considering large variations in structural organization of mitochondria and the cytoskeleton among cells, we used very large sample sizes despite significant technical challenges. At least two independent experiments have been done to confirm consistency of results. All repetitive experiments gave consistent results. Numerical data sets were first evaluated for normality by Kolmogorov-Smirnov test. For the normally distributed values, two-tailed t-test was used to compare two data sets and Welch’s Anova test with posthoc Games-Howell test was used for multiple comparisons. For not normally distributed values, Mann-Whitney test

was used to compare two unpaired data sets, Wilcoxon test was used to compare two paired data sets, and Kruskal-Wallis with posthoc Dunn's test was used for multiple comparisons.

Data availability

Source data for Figures 5h, 6b, 7b and statistical results presented in the text have been provided as Supplementary Table 1. All other data supporting the findings of this study are available from the corresponding author on reasonable request.

Supplementary Material

Refer to Web version on PubMed Central for supplementary material.

Acknowledgements

We thank Henry N. Higgs for helpful discussions and gifts of reagents, Andrew York and Michael Schell for the gifts of reagents and the members of the Svitkina lab, Maria Shutova and Nadia Efimova, for comments on the manuscript. This work was supported by National Institutes of Health grants R01 GM 095977 and R01 GM 106000 to T.M.S.

References

1. Friedman JR & Nunnari J Mitochondrial form and function. Nature 505, 335–343, doi:10.1038/nature12985 (2014). [PubMed: 24429632]
2. Mishra P & Chan DC Mitochondrial dynamics and inheritance during cell division, development and disease. Nat Rev Mol Cell Biol 15, 634–646, doi:10.1038/nrm3877 (2014). [PubMed: 25237825]
3. Wai T & Langer T Mitochondrial dynamics and metabolic regulation. Trends Endocrinol Metab 27, 105–117, doi:10.1016/j.tem.2015.12.001 (2016). [PubMed: 26754340]
4. Pagliuso A, Cossart P & Stavru F The ever-growing complexity of the mitochondrial fission machinery. Cell Mol Life Sci 75, 355–374, doi:10.1007/s00018-017-2603-0 (2018). [PubMed: 28779209]
5. Ramachandran R Mitochondrial dynamics: The dynamin superfamily and execution by collusion. Semin Cell Dev Biol 76, 201–212, doi:10.1016/j.semcdb.2017.07.039 (2018). [PubMed: 28754444]
6. Lee JE, Westrate LM, Wu H, Page C & Voeltz GK Multiple dynamin family members collaborate to drive mitochondrial division. Nature 540, 139–143, doi:10.1038/nature20555 (2016). [PubMed: 27798601]
7. Basu K et al. Molecular mechanism of DRP1 assembly studied in vitro by cryo-electron microscopy. PLoS One 12, e0179397, doi:10.1371/journal.pone.0179397 (2017). [PubMed: 28632757]
8. Francy CA, Alvarez FJ, Zhou L, Ramachandran R & Mears JA The mechanoenzymatic core of dynamin-related protein 1 comprises the minimal machinery required for membrane constriction. J Biol Chem 290, 11692–11703, doi:10.1074/jbc.M114.610881 (2015). [PubMed: 25770210]
9. Macdonald PJ et al. Distinct splice variants of dynamin-related protein 1 differentially utilize mitochondrial fission factor as an effector of cooperative GTPase activity. J Biol Chem 291, 493–507, doi:10.1074/jbc.M115.680181 (2016). [PubMed: 26578513]
10. Korobova F, Ramabhadran V & Higgs HN An actin-dependent step in mitochondrial fission mediated by the ER-associated formin INF2. Science 339, 464–467, doi:10.1126/science.1228360 (2013). [PubMed: 23349293]
11. Friedman JR et al. ER tubules mark sites of mitochondrial division. Science 334, 358–362, doi:10.1126/science.1207385 (2011). [PubMed: 21885730]
12. Manor U et al. A mitochondria-anchored isoform of the actin-nucleating Spire protein regulates mitochondrial division. Elife 4, e08828, doi:10.7554/eLife.08828 (2015).

13. DuBoff B, Gotz J & Feany MB Tau promotes neurodegeneration via DRP1 mislocalization in vivo. Neuron 75, 618–632, doi:10.1016/j.neuron.2012.06.026 (2012). [PubMed: 22920254]
14. Korobova F, Gauvin TJ & Higgs HN A role for myosin II in mammalian mitochondrial fission. Curr Biol 24, 409–414, doi:10.1016/j.cub.2013.12.032 (2014). [PubMed: 24485837]
15. Svitkina T The actin cytoskeleton and actin-based motility. Cold Spring Harb Perspect Biol 10, a018267, doi:10.1101/cshperspect.a018267 (2018). [PubMed: 29295889]
16. Li S et al. Transient assembly of F-actin on the outer mitochondrial membrane contributes to mitochondrial fission. J Cell Biol 208, 109–123, doi:10.1083/jcb.201404050 (2015). [PubMed: 25547155]
17. Hatch AL, Gurel PS & Higgs HN Novel roles for actin in mitochondrial fission. J Cell Sci 127, 4549–4560, doi:10.1242/jcs.153791 (2014). [PubMed: 25217628]
18. Cheffings TH, Burroughs NJ & Balasubramanian MK Actomyosin ring formation and tension generation in eukaryotic cytokinesis. Curr Biol 26, R719–R737, doi:10.1016/j.cub.2016.06.071 (2016). [PubMed: 27505246]
19. Billington N, Wang A, Mao J, Adelstein RS & Sellers JR Characterization of three full-length human nonmuscle myosin II paralogs. J Biol Chem 288, 33398–33410, doi:10.1074/jbc.M113.499848 (2013). [PubMed: 24072716]
20. Verkhovsky AB, Svitkina TM & Borisy GG Myosin II filament assemblies in the active lamella of fibroblasts: their morphogenesis and role in the formation of actin filament bundles. J Cell Biol 131, 989–1002 (1995). [PubMed: 7490299]
21. Requejo-Isidro J Fluorescence nanoscopy. Methods and applications. J Chem Biol 6, 97–120, doi:10.1007/s12154-013-0096-3 (2013). [PubMed: 24432127]
22. Svitkina TM Platinum replica electron microscopy: Imaging the cytoskeleton globally and locally. Int J Biochem Cell Biol 86, 37–41, doi:10.1016/j.biocel.2017.03.009 (2017). [PubMed: 28323208]
23. Collins A, Warrington A, Taylor KA & Svitkina T Structural organization of the actin cytoskeleton at sites of clathrin-mediated endocytosis. Curr Biol 21, 1167–1175, doi:10.1016/j.cub.2011.05.048 (2011). [PubMed: 21723126]
24. Korobova F & Svitkina T Molecular architecture of synaptic actin cytoskeleton in hippocampal neurons reveals a mechanism of dendritic spine morphogenesis. Mol Biol Cell 21, 165–176 (2010). [PubMed: 19889835]
25. Svitkina TM et al. Mechanism of filopodia initiation by reorganization of a dendritic network. J Cell Biol 160, 409–421 (2003). [PubMed: 12566431]
26. Svitkina TM & Borisy GG in Cell Biology: A Laboratory Handbook; 3rd Edition Vol. 3 (ed Celis Julio) 277–285 (Elsevier, 2006).
27. Svitkina T Electron microscopic analysis of the leading edge in migrating cells. Methods Cell Biol 79, 295–319, doi:10.1016/S0091-679X(06)79012-4 (2007). [PubMed: 17327162]
28. Svitkina T Imaging cytoskeleton components by electron microscopy. Methods Mol Biol 1365, 99–118, doi:10.1007/978-1-4939-3124-8_5 (2016). [PubMed: 26498781]
29. Yang C et al. Novel roles of formin mDia2 in lamellipodia and filopodia formation in motile cells. PLoS Biol 5, e317 (2007). [PubMed: 18044991]
30. Heuser J The production of ‘cell cortices’ for light and electron microscopy. Traffic 1, 545–552 (2000). [PubMed: 11208142]
31. Sato F, Asakawa H, Fukuma T & Terada S Semi-in situ atomic force microscopy imaging of intracellular neurofilaments under physiological conditions through the ‘sandwich’ method. Microscopy (Oxf) 65, 316–324, doi:10.1093/jmicro/dfw006 (2016). [PubMed: 26960670]
32. Efimova N & Svitkina TM Branched actin networks push against each other at adherens junctions to maintain cell-cell adhesion. J Cell Biol 217, 1827–1845, doi:10.1083/jcb.201708103 (2018). [PubMed: 29507127]
33. Gurel PS et al. Assembly and turnover of short actin filaments by the formin INF2 and profilin. J Biol Chem 290, 22494–22506, doi:10.1074/jbc.M115.670166 (2015). [PubMed: 26124273]
34. Smirnova E, Griparic L, Shurland DL & van der Bliek AM Dynamin-related protein Drp1 is required for mitochondrial division in mammalian cells. Mol Biol Cell 12, 2245–2256 (2001). [PubMed: 11514614]

35. De Vos KJ, Allan VJ, Grierson AJ & Sheetz MP Mitochondrial function and actin regulate dynamin-related protein 1-dependent mitochondrial fission. Curr Biol 15, 678–683, doi:10.1016/j.cub.2005.02.064 (2005). [PubMed: 15823542]

36. Ji WK, Hatch AL, Merrill RA, Strack S & Higgs HN Actin filaments target the oligomeric maturation of the dynamic GTPase Drp1 to mitochondrial fission sites. Elife 4, e11553, doi:10.7554/eLife.11553 (2015). [PubMed: 26609810]

37. Ramabhadran V, Hatch AL & Higgs HN Actin monomers activate inverted formin 2 by competing with its autoinhibitory interaction. J Biol Chem 288, 26847–26855, doi:10.1074/jbc.M113.472415 (2013). [PubMed: 23921379]

38. Barsoum MJ et al. Nitric oxide-induced mitochondrial fission is regulated by dynamin-related GTPases in neurons. Embo J 25, 3900–3911, doi:10.1038/sj.emboj.7601253 (2006). [PubMed: 16874299]

39. Toyama EQ et al. Metabolism. AMP-activated protein kinase mediates mitochondrial fission in response to energy stress. Science 351, 275–281, doi:10.1126/science.aab4138 (2016). [PubMed: 26816379]

40. Sanmartin CD et al. Ryanodine receptor-mediated Ca(2+) release underlies iron-induced mitochondrial fission and stimulates mitochondrial Ca(2+) uptake in primary hippocampal neurons. Front Mol Neurosci 7, 13, doi:10.3389/fnmol.2014.00013 (2014). [PubMed: 24653672]

41. Wales P et al. Calcium-mediated actin reset (CaAR) mediates acute cell adaptations. Elife 5, e19850, doi:10.7554/eLife.19850 (2016). [PubMed: 27919320]

42. Bao J, Jana SS & Adelstein RS Vertebrate nonmuscle myosin II isoforms rescue small interfering RNA-induced defects in COS-7 cell cytokinesis. J Biol Chem 280, 19594–19599, doi:10.1074/jbc.M501573200 (2005). [PubMed: 15774463]

43. Shutova MS et al. Self-sorting of nonmuscle myosins IIA and IIB polarizes the cytoskeleton and modulates cell motility. J Cell Biol 216, 2877–2889, doi:10.1083/jcb.201705167 (2017). [PubMed: 28701425]

44. Helle SCJ et al. Mechanical force induces mitochondrial fission. Elife 6, e30292, doi:10.7554/eLife.30292 (2017). [PubMed: 29119945]

45. Ban-Ishihara R, Ishihara T, Sasaki N, Mihara K & Ishihara N Dynamics of nucleoid structure regulated by mitochondrial fission contributes to cristae reformation and release of cytochrome c. Proc Natl Acad Sci U S A 110, 11863–11868, doi:10.1073/pnas.1301951110 (2013). [PubMed: 23821750]

46. Bogenhagen DF, Wang Y, Shen EL & Kobayashi R Protein components of mitochondrial DNA nucleoids in higher eukaryotes. Mol Cell Proteomics 2, 1205–1216, doi:10.1074/mcp.M300035-MCP200 (2003). [PubMed: 14514796]

47. Garrido N et al. Composition and dynamics of human mitochondrial nucleoids. Mol Biol Cell 14, 1583–1596, doi:10.1091/mbc.e02-07-0399 (2003). [PubMed: 12686611]

48. Chakrabarti R et al. INF2-mediated actin polymerization at the ER stimulates mitochondrial calcium uptake, inner membrane constriction, and division. J Cell Biol 217, 251–268, doi:10.1083/jcb.201709111 (2018). [PubMed: 29142021]

49. Cho B et al. Constriction of the mitochondrial inner compartment is a priming event for mitochondrial division. Nat Commun 8, 15754, doi:10.1038/ncomms15754 (2017). [PubMed: 28598422]

References

50. Wilcox KS, Buchhalter J & Dichter MA Properties of inhibitory and excitatory synapses between hippocampal neurons in very low density cultures. Synapse 18, 128–151 (1994). [PubMed: 7839312]

51. Efimova N et al. betaIII spectrin is necessary for formation of the constricted neck of dendritic spines and regulation of synaptic activity in neurons. J Neurosci 37, 6442–6459, doi:10.1523/JNEUROSCI.3520-16.2017 (2017). [PubMed: 28576936]

52. Svitkina TM & Borisy GG Correlative light and electron microscopy of the cytoskeleton of cultured cells. Methods Enzymol 298, 570–592, doi:10.1016/S0076-6879(98)98045-4 (1998). [PubMed: 9751908]

53. Svitkina T Imaging cytoskeleton components by electron microscopy. Methods Mol Biol 1365, 99–118, doi:10.1007/978-1-4939-3124-8_5 (2016). [PubMed: 26498781]

54. Shutova MS et al. Self-sorting of nonmuscle myosins IIA and IIB polarizes the cytoskeleton and modulates cell motility. J Cell Biol 216, 2877–2889, doi:10.1083/jcb.201705167 (2017). [PubMed: 28701425]

55. York AG et al. Instant super-resolution imaging in live cells and embryos via analog image processing. Nat Methods 10, 1122–1126, doi:10.1038/nmeth.2687 (2013). [PubMed: 24097271]

56. Strack S, Wilson TJ & Cribbs JT Cyclin-dependent kinases regulate splice-specific targeting of dynamin-related protein 1 to microtubules. J Cell Biol 201, 1037–1051, doi:10.1083/jcb.201210045 (2013). [PubMed: 23798729]

57. Johnson HW & Schell MJ Neuronal IP3 3-kinase is an F-actin-bundling protein: role in dendritic targeting and regulation of spine morphology. Mol Biol Cell 20, 5166–5180 (2009). [PubMed: 19846664]

58. Dulyaninova NG, House RP, Betapudi V & Bresnick AR Myosin-IIA heavy-chain phosphorylation regulates the motility of MDA-MB-231 carcinoma cells. Mol Biol Cell 18, 3144–3155, doi:10.1091/mbc.E06-11-1056 (2007). [PubMed: 17567956]

59. Wei Q & Adelstein RS Conditional expression of a truncated fragment of nonmuscle myosin II-A alters cell shape but not cytokinesis in HeLa cells. Mol Biol Cell 11, 3617–3627 (2000). [PubMed: 11029059]

60. Ramabhadran V, Hatch AL & Higgs HN Actin monomers activate inverted formin 2 by competing with its autoinhibitory interaction. J Biol Chem 288, 26847–26855, doi:10.1074/jbc.M113.472415 (2013). [PubMed: 23921379]

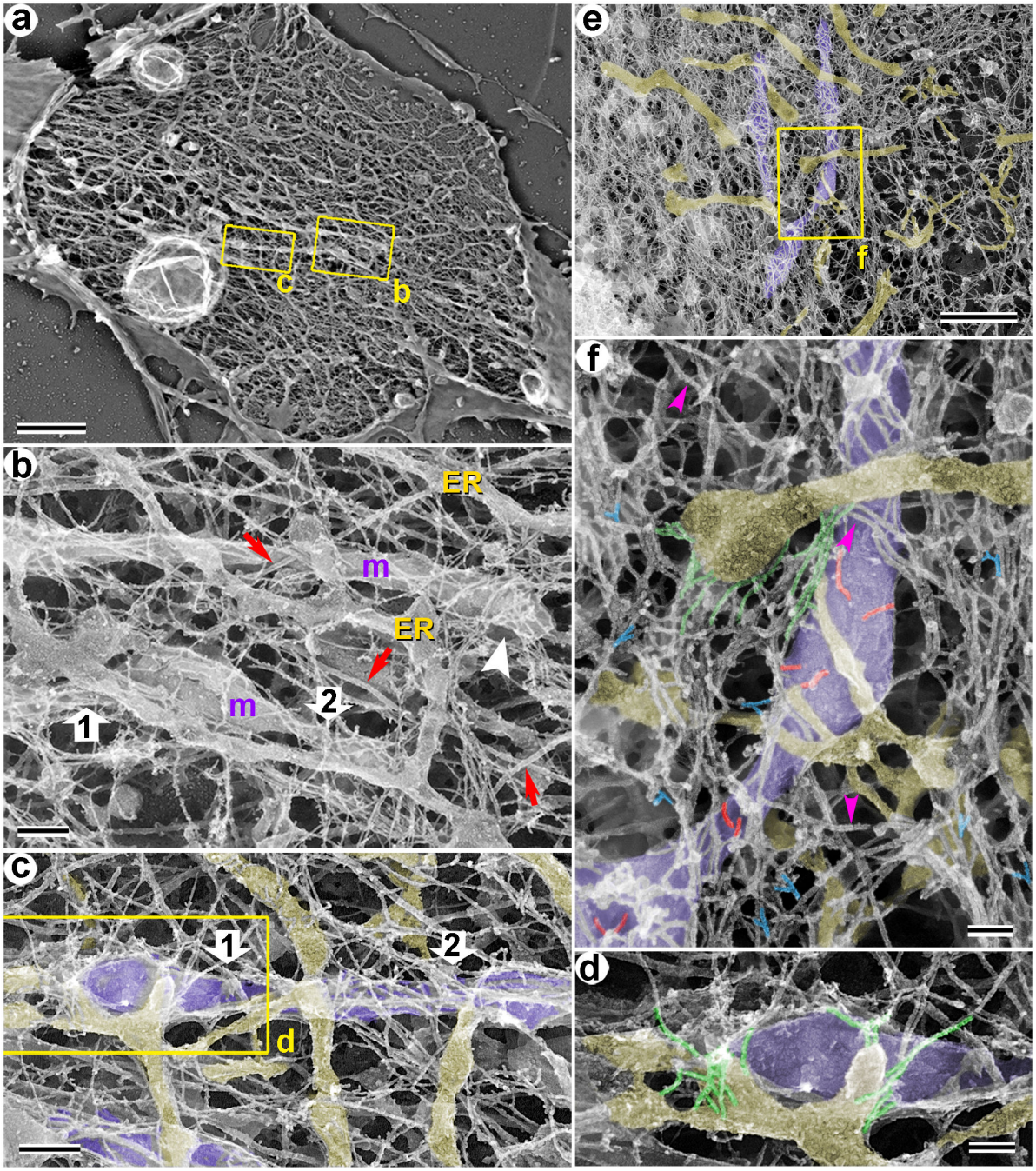

Fig. 1: Ultrastructure of the cell interior in glial cells revealed by PREM.

(a-d) Exposure of the cell interior by saponin extraction. See additional examples in Supplemental Fig. 1.

(a) A broad window in the apical plasma membrane reveals both membrane organelles and the cytoskeleton in the cell interior. Boxed regions are zoomed in panels b and c.

(b-d) Organization of the cytoskeleton in the vicinity of mitochondria (m) and the ER (ER).

(b) Mitochondrial constrictions (white arrows) are associated with a slightly increased density of associated actin filaments. Constriction #1 is intersected by an ER tubule, while

constriction #2 has the nearest ER tubule at some distance. The upper mitochondrion has no prominent constrictions and interacts with filaments relatively uniformly along the length, except for the tip (arrowhead), which associates with a relatively dense actin filament array. Red arrows point to microtubules. See a 3D version of this image with pseudocolored mitochondria and ER in Supplementary Fig. 1c.

(c) An elongated mitochondrial constriction between arrows 1 and 2 is associated with intersecting actin filaments and ER tubules. Putative mitochondria and the ER are pseudocolored in purple and yellow, respectively. See a 3D version of this image in Supplementary Fig.1d. Boxed region is enlarged in d.

(d) Some actin filaments (pseudocolored green) originate from the ER surface (yellow) and eventually intersect the mitochondrion (purple).

(e, f) Exposure of the cell interior by nitrocellulose-mediated unroofing. Putative mitochondria and the ER are pseudocolored purple and yellow, respectively. Boxed region in e is enlarged in f. See additional examples in Supplementary Fig. 1.

(f) Some actin filaments (green) originate from the ER tubule (yellow), continue downward and intersect the mitochondrion (purple) at the constriction site. A few actin filaments (red) appear to originate at the mitochondrial surface. Magenta arrowheads point to intermediate filaments. Branched actin filaments in the interstitial network are shaded blue.

Scale bars: 2 μm (a), 200 nm (b and c), 100 nm (d and f) and 1 μm (e). The images are representative of $n = 6$ independent experiments, which gave similar results.

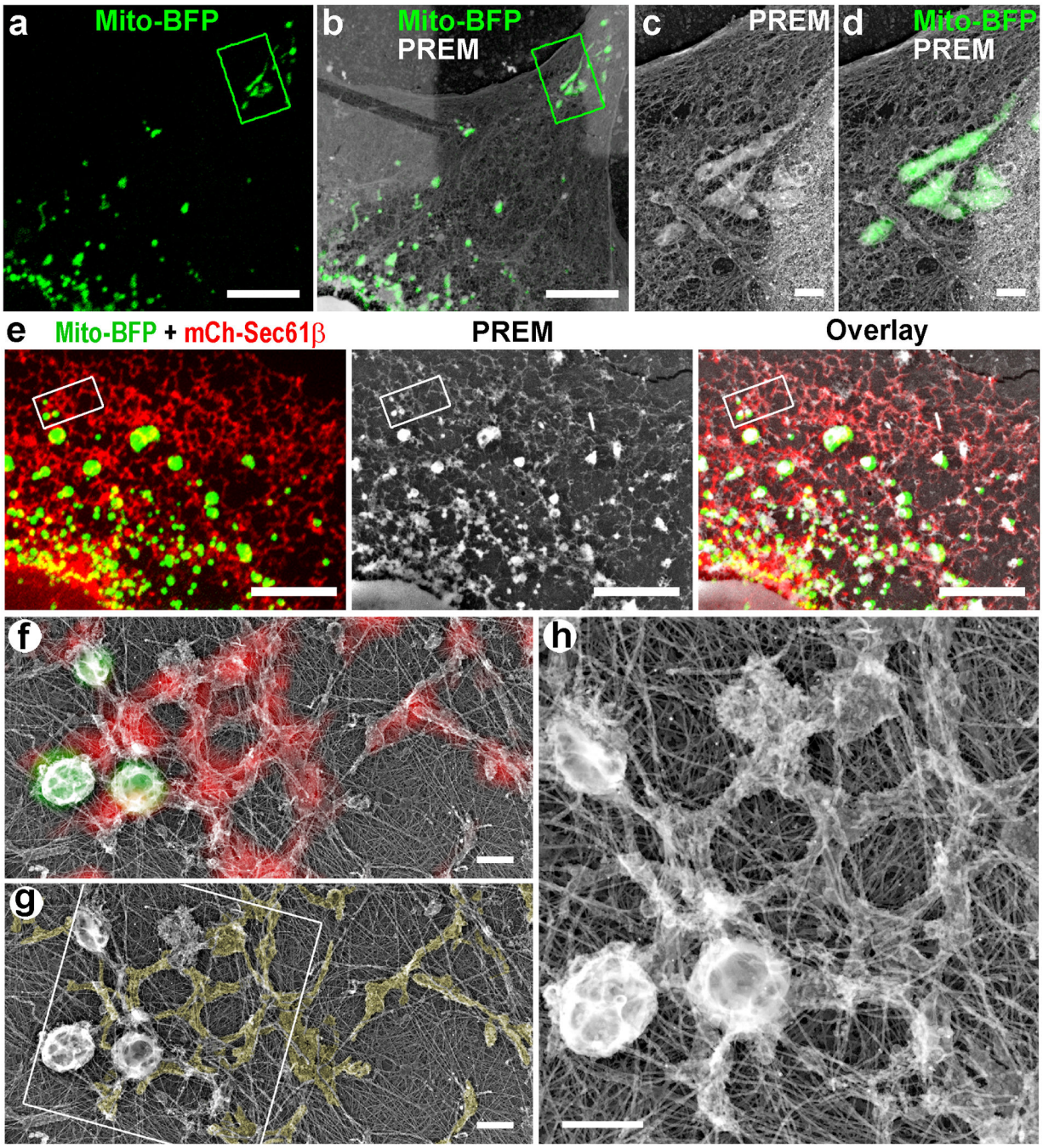

Figure 2: CLEM of COS-7 cells.

(a-d) CLEM of a COS-7 cell expressing a mitochondrial marker Mito-BFP.

(a) Fluorescence microscopy of Mito-BFP (green) in the cell after unroofing.

(b) Overlay of Mito-BFP fluorescence and PREM of the same cell.

(c, d) PREM (c) and fluorescence/PREM overlay (d) images of the boxed region in B.

(e-h) CLEM of COS-7 cell expressing Mito-BFP and mCherry-Sec61β.

(e) Unroofed cell expressing Mito-BFP (green) and mCherry-Sec61β (red) shown by fluorescence microscopy (left), PREM (middle) and as fluorescence/PREM overlay (right).

(f, g) Enlarged boxed region from E shown as fluorescence/PREM overlay (f) or as PREM with visually identified ER shaded in yellow (g).

(e) Enlarged boxed region in g.

Scale bars: 10 μm (a and e), 1 μm (c and d) and 500 nm (f-h). The images are representative of $n = 2$ independent experiments, which gave similar results.

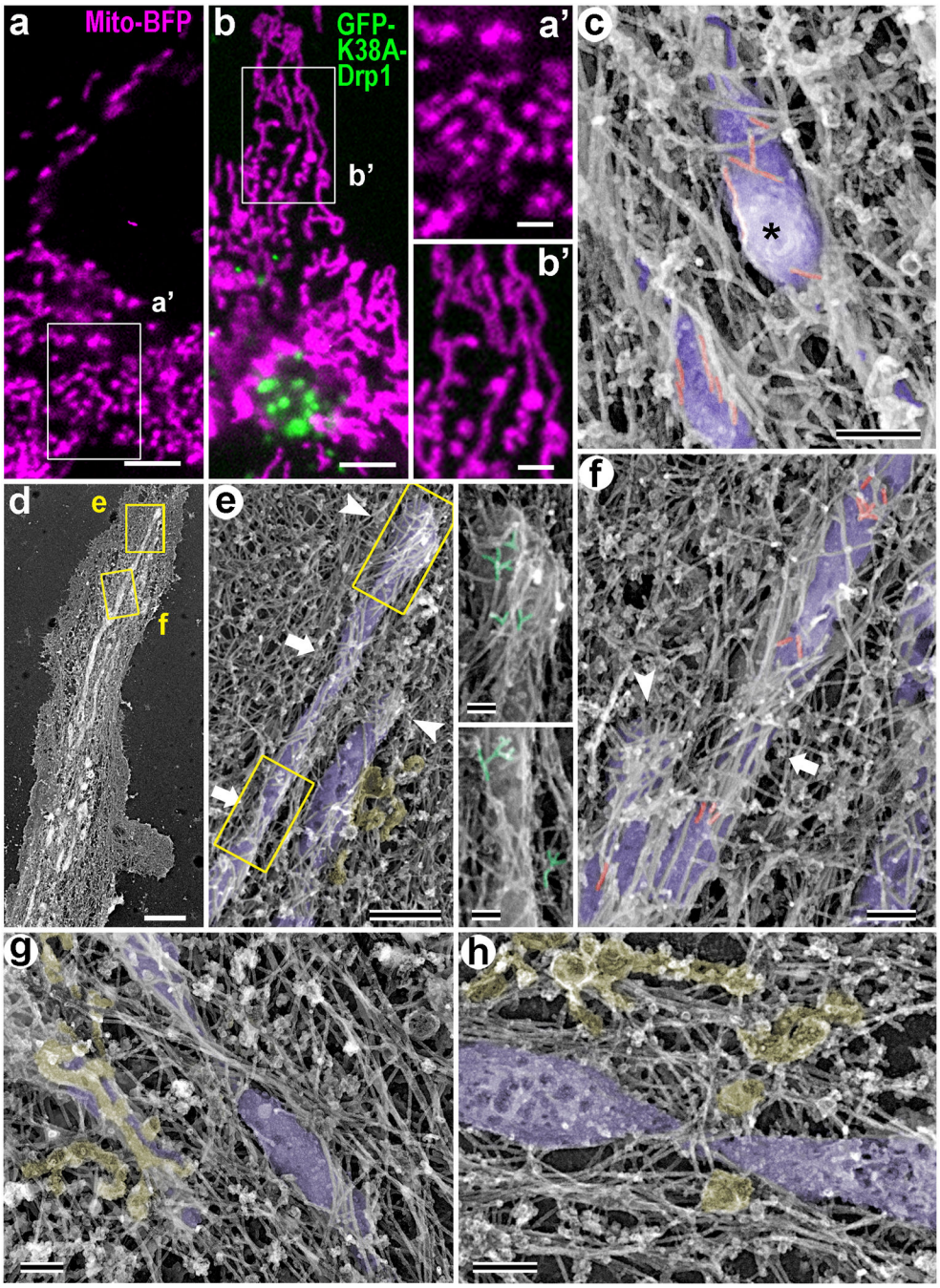

Figure 3: Actin filament organization at mitochondrial constriction sites induced in COS-7 cells by expression of the dominant negative GFP-K38A-Drp1 construct.

(a, b) Confocal microscopy of COS-7 expressing mitochondrial marker Mito-BFP (magenta) either alone (a) or together with GFP-K38A-Drp1 (green) (b). Boxed regions are zoomed in a' and b', respectively. GFP-K38A-Drp1 expression results in elongation of mitochondria. (c-h) PREM of unroofed GFP-K38A-Drp1-expressing COS-7 cells. Mitochondria and putative ER structures are color-coded in purple and yellow, respectively.

(c) PREM showing a bulging mitochondrial region (asterisk) between adjacent constriction sites. See 3D version of this image in Supplementary Fig. 4.

(d-f) Overview of an unroofed cell (d) and enlargements of boxed regions (e and f) from this cell. Mitochondrial constrictions (e, f, arrows) and mitochondrial tips (e, f, arrowheads) are associated with accumulations of actin filaments, which form a criss-cross pattern at constrictions. Most actin filaments are unbranched, but some branched filaments (green in right panels in e) are also present. Boxed regions in e are enlarged at right.
(g, h) Additional examples of mitochondrial constrictions associated with criss-cross pattern of actin filaments. See animated series of tilt images for panel h in Supplementary Video 1. Scale bars: 5 μm (a and b), 2 μm (a', b', and d), 200 nm (c, f-h), 500 nm (e) and 100 nm (e, insets). The images are representative of $n = 3$ independent experiments, which gave similar results.

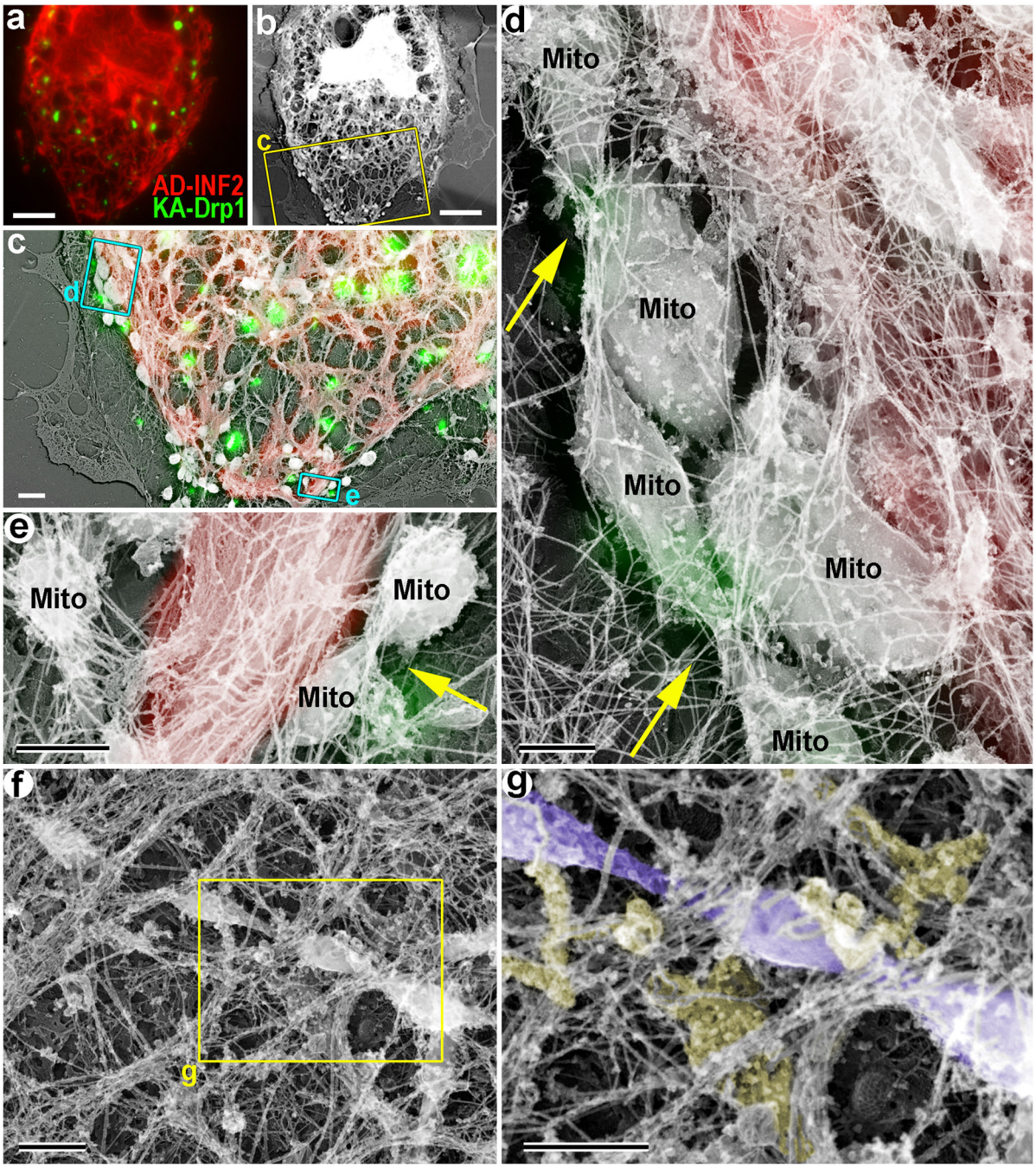

Figure 4: Actin filament organization at mitochondrial constriction sites formed in COS-7 cells coexpressing dominant negative GFP-K38A-Drp1 (KA-Drp1) and constitutively active mCherry-INF2-A149D-CAAX (AD-INF2).

(a-e) CLEM of a double-expressing COS-7 cell.

(a, b) Fluorescence (a) and PREM (b) images of the same cell.

(c) Fluorescence/PREM overlay of the boxed region in b.

(d, e) Enlarged boxed regions from C overlaid with fluorescence signals from mCherry-INF2-A149D-CAAX (red) and GFP-K38A-Drp1 (green). The INF2-positive ER (red) is

covered by abundant actin filaments, some of which extend toward mitochondrial constrictions (arrows) marked by GFP-K38A-DRP1 spots (green). Mito, mitochondria. (f, g) Additional PREM example of unroofed COS-7 cell coexpressing mCherry-INF2-A149D-CAAX and GFP-K38A-Drp1 shows a long mitochondrion with several constrictions intersected with multiple actin filaments. Boxed region in F is enlarged in G. Putative mitochondria and the ER are pseudocolored in purple and yellow, respectively. See 3D version of panel f in Supplementary Fig. 4.

Scale bars: 10 μm (A and B), 2 μm (C) and 500 nm (D-G). The images are representative of $n = 2$ independent experiments, which gave similar results.

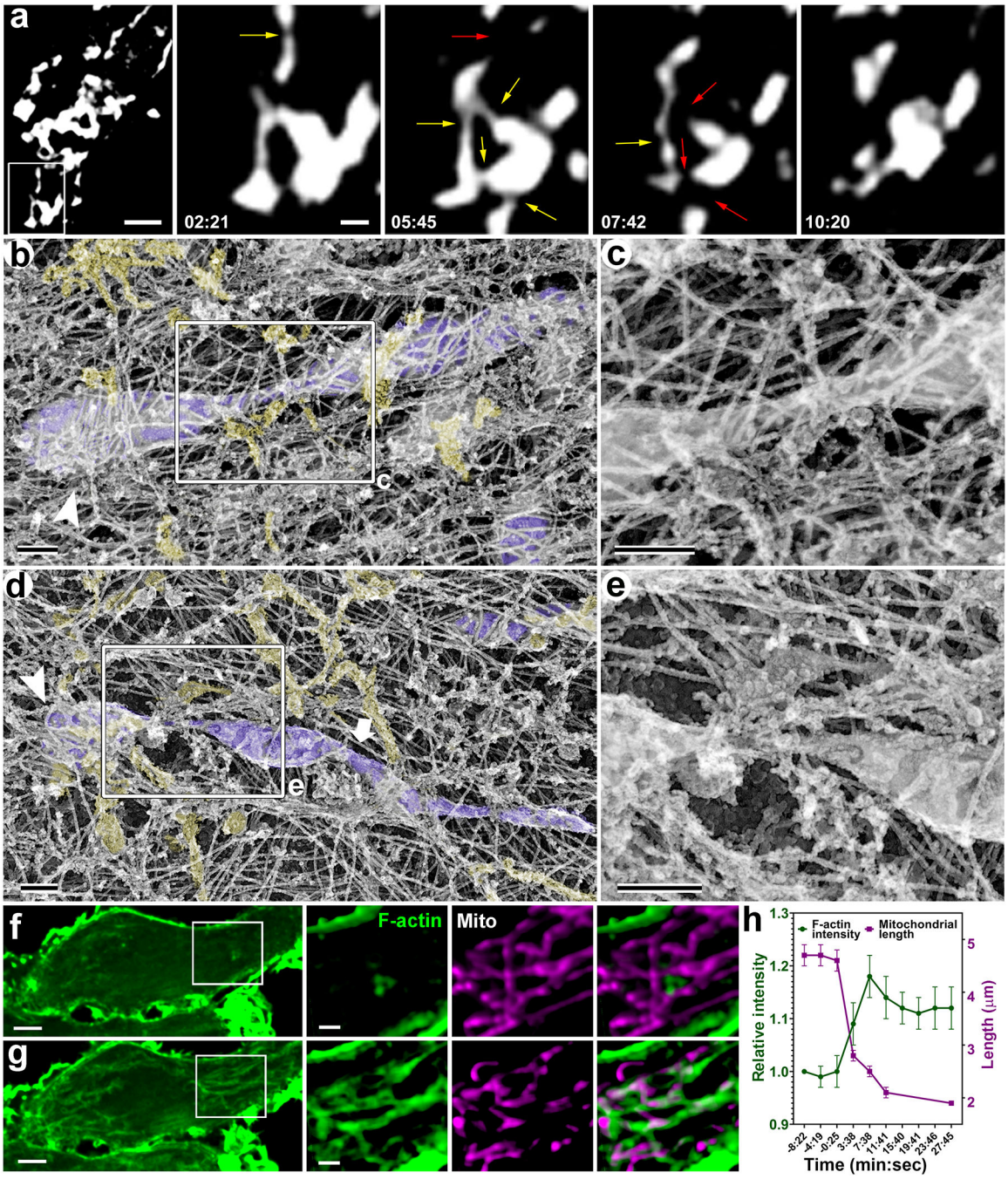

Figure 5: Rotenone treatment induces mitochondrial fission and actin reorganization in cells.

(a) Time course of rotenone-induced mitochondrial constriction (yellow arrows) and fission (red arrows) in a glial cell expressing a mitochondrial marker Tom20-mCherry and exposed to rotenone at time 0:00. Left panel: Overview of the cell at t=2:21. Right panels: time lapse sequence of the boxed region. Time (min:sec) is shown after rotenone addition.

(b, d) PREM images of constricted mitochondria (purple) in unroofed glial cells treated with rotenone for 8 min. Membranous structures likely representing the ER are shaded yellow. Actin filaments from the relatively dense surrounding network intersect the constriction sites

(boxed regions) or enwrap the mitochondrial ends (arrowheads). Boxed regions are enlarged in c and e, respectively.

(f, g) Confocal microscopy of HeLa cells coexpressing GFP-Ftractin (green) and Mito-BFP (magenta) before (f) and 2 min 32 sec after (g) rotenone treatment. Left panels: Midplane confocal slices of the Ftractin fluorescence showing an increase in the cytosolic F-actin after rotenone treatment. Right panels: Enlarged boxed regions show partial colocalization of mitochondria and F-actin. Mitochondrial fission after rotenone treatment is also evident.

(h) Relative mean fluorescence intensity of GFP-Ftractin (green, left Y-axis) and the average mitochondrial length (purple, right Y-axis) over time in rotenone-treated HeLa cells. Rotenone was added at time 0. Average fluorescence intensity of GFP-Ftractin from 10 cells was normalized against the pretreatment values for individual cells. Mitochondrial lengths were measured for ~100 to ~400 mitochondria per time point from 10 cells. Error bars, SEM. Scale bars: 5 μm (a, left), 1 μm (a, right), 200 nm (b-e). 5 μm (f and g, left) and 2 μm (f and g, right). The images are representative of $n = 2$ independent experiments, which gave similar results.

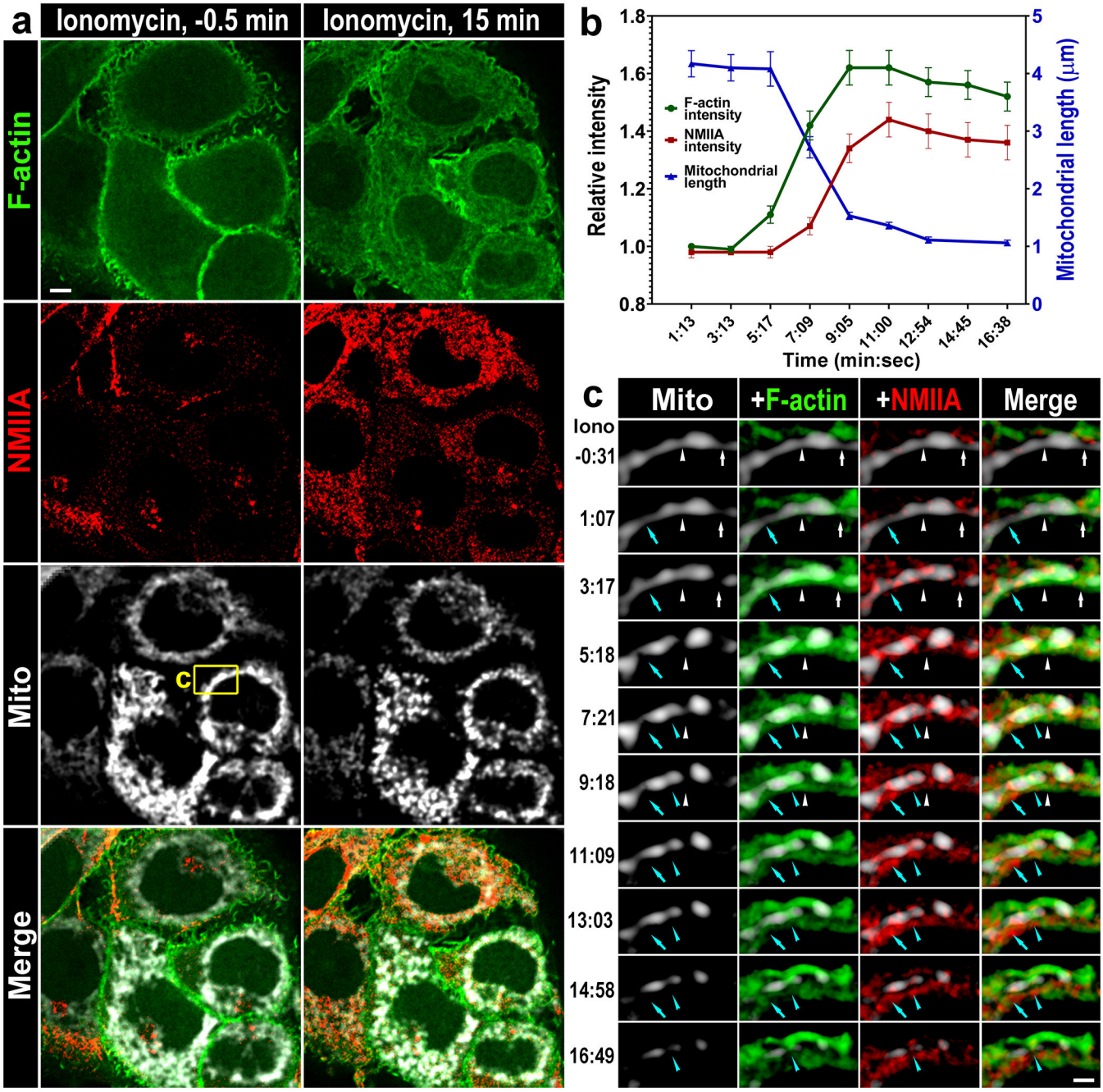

Figure 6: Dynamics of F-actin and NMIIA in the course of ionomycin-induced mitochondrial fission in HeLa cells.

(a) Midplane confocal slice of cells expressing GFP-Ftractin (F-actin, green), mCherry-NMIIA (NMIIA, red) and Mito-BFP (Mito, white) before (left) and after (right) ionomycin addition. Fluorescence intensities of both GFP-Ftractin and mCherry-NMIIA in the internal cytoplasm increase after ionomycin application, while mitochondria undergo fission.

(b) Relative mean fluorescence intensity (left Y-axis) of GFP-Ftractin (green) and mCherry-NMIIA (red) in the internal cytoplasm (n=37 regions from 15 cells for each marker) and the mitochondrial length (blue, right Y-axis, n=34 individual mitochondria monitored over time

from 5 cells) over time in the course of ionomycin treatment. Error bars: SEM. Data show one representative experiment out of two. The second experiment gave qualitatively similar results but was not quantified.

(c) Detailed time course of the boxed region in A showing dynamics of Mito-BFP (Mito, white), GFP-Ftractin (F-actin, green) and mCherry-NMIIA (NMIIA, red) during mitochondria fission after application of ionomycin at time 0:00 (min:sec). Initiation of mitochondrial constriction is accompanied by appearance of F-actin and, occasionally, NMIIA clouds intersecting the constriction (arrows and arrowheads). Subsequently, F-actin remains at the constriction sites until mitochondrial fission, whereas NMIIA mostly fluctuates in the mitochondrion vicinity.

Scale bars: 5 μm (a) and 1 μm (c). The images are representative of $n = 2$ independent experiments, which gave similar results.

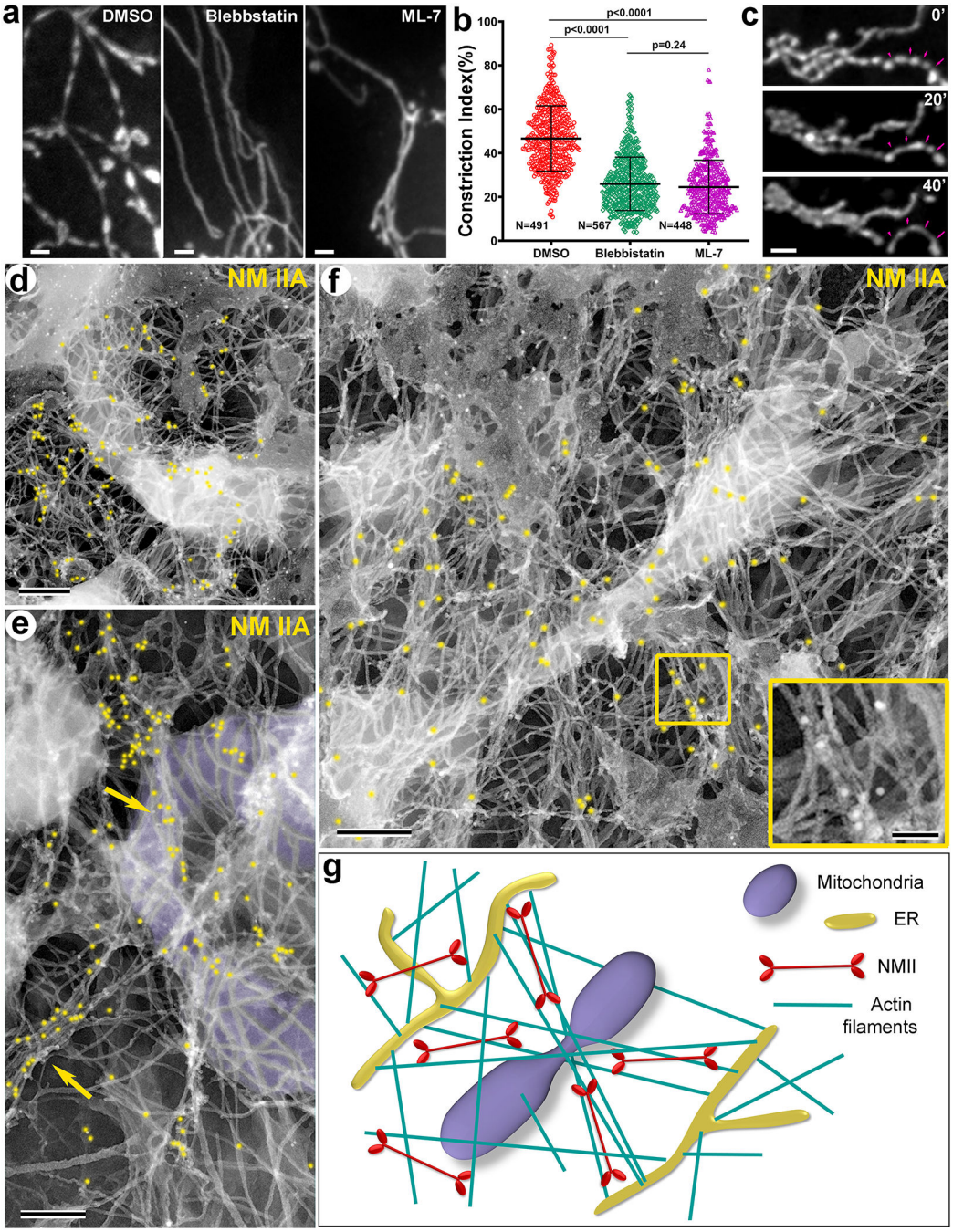

Figure 7: NMII associated with interstitial actin network stimulates mitochondrial constrictions.

(a-c) Inhibition of NMII activity causes relaxation of mitochondrial constrictions in K38A-Drp1-expressing COS-7 cells.

(a) COS-7 cells expressing GFP-K38A-Drp1 and Mito-BFP were treated for 1 hour with DMSO (left), 50 μM blebbistatin (middle) or 50 μM ML-7 (right). The images are representative of $n = 2$ independent experiments with similar results.

(b) Quantification of the constriction index (a degree of invagination) for individual constrictions in conditions shown in A. Thick and thin lines represent mean and SD,

respectively. N=491 constrictions from 16 DMSO-treated cells, 567 constrictions from 10 blebbistatin-treated cells and 448 constrictions from 10 ML-7-treated cells ($n = 2$ independent experiments with similar results). P-values were determined by Kruskal-Wallis test with posthoc Dunn's test; normality was determined by Kolmogorov-Smirnov test.
(c) Time frames of COS-7 cells expressing GFP-K38A-Drp1 and labelled with MitoTracker DeepRed in the course of treatment with 75 μM ML-7. Time is shown relative to ML-7 addition. Magenta arrowheads mark individual constrictions that relax over time. The images are representative of $n = 2$ independent experiments with similar results.
(d-f) Immunogold PREM of NMIIA localization at mitochondrial constrictions in HeLa cells treated with ionomycin for 2 min. Immunogold particles (12 nm) are marked by yellow dots. Some NMIIA enrichment is seen on actin filaments intersecting the constriction (arrows in e and boxed region in f). Inset in F shows an enlarged boxed region with uncolorized gold particles.
Scale bars: 2 μm (a,c), 200 nm (d-f) and 50 nm (inset in f). The images are representative of $n = 2$ independent experiments with similar results.
(g) Model of actin-NMII dependent mitochondrial constriction. Mitochondria and the ER are embedded into interstitial actin network that includes many actin filaments nucleated at the ER by INF2-CAAX. NMII filaments within the interstitial network cause stochastic distortions of the network, thereby applying pressure onto mitochondria trapped in the network. Indentations on the mitochondrial surface that result from mechanical activity of the actin-NMII interstitial network eventually develop into constrictions in an Mff-dependent manner and lead to Drp1-mediated fission. See text for detail.